Catalysis Science & Technology

ROYAL SOCIETY OF CHEMISTRY

PAPER

View Article Online
View Journal | View Issue

Cite this: *Catal. Sci. Technol.*, 2024, 14, 1318

Operando UV-vis spectroscopy for real-time monitoring of nanoparticle size in reaction conditions: a case study on *r*WGS over Au nanoparticles†

Chiara Negri, [a] Riccardo Colombo, [a] Mauro Bracconi, [a] Cesare Atzori, [b] Alessandro Donazzi, [a] Andrea Lucotti, [c] Matteo Tommasini [c] and Matteo Maestri *[a]

Received 6th October 2023,
Accepted 27th January 2024

DOI: 10.1039/d3cy01392h

rsc.li/catalysis

We propose the use of surface plasmon resonance (SPR) as a distinctive marker for real-time monitoring in reaction conditions of gold nanoparticles supported on α-Al_2O_3. The study leverages the SPR shape-and-size dependency to monitor metal nanoparticles in reaction conditions, evidencing an influence of both dimensions and agglomerations on the SPR peak position. *Operando* measurements, coupling UV-vis spectroscopy and catalytic testing, allows to follow the dynamics during nanoparticle formation (Au^{3+} to Au^0 reduction) and during the reverse water gas shift reaction ($CO_2 + H_2 \rightarrow CO + H_2O$). The catalyst structure and stability in reaction conditions was further confirmed by *operando* X-ray spectroscopy and PXRD data. Overall, this approach enables the direct acquisition of information on the structure–activity relationship of metal-based supported catalysts under actual reaction conditions.

1 Introduction

Heterogeneous catalysis nowadays plays a pivotal role in the chemical sector, in energy applications and for environmental protection. The constant demand for more efficient and sustainable processes and resource exploitation calls for increasing efforts to improve the catalytic processes for a more viable future. This is a key-challenge in reaction engineering and requires a deep knowledge of the catalyst functionality at atomistic level, to enable a rational design of both optimized processes and new materials.[1,2] In this scenario it is fundamental to acknowledge the "living character" of heterogeneous catalyst under the reacting environment, that is, the dynamic change in its structure during the reaction as a function of the operating conditions.[3,4] Specifically, this is crucial for supported metal-based catalysts, where nanoparticles can change their size and shape depending on the applied conditions, thus varying the available active sites and affecting the overall catalytic performances.[5,6] As a consequence, to gain a full comprehension of the catalyst functioning under real working conditions, it is necessary to assess the actual nanoparticles morphology and to correlate it with the observed macroscopic kinetic results.[7,8] Currently, the state-of-the-art approach to assess the structure of supported metal-based catalysts applies techniques operating at conditions significantly different from the reacting environment of kinetic analysis (*i.e.* high vacuum, low temperature *vs.* high pressure, high temperature). These *ex situ* characterization methods (*i.e.* HR-TEM, H_2 and CO chemisorption, FT-IR spectroscopy with probe molecules[9,10]) allow for the study of nanoparticle morphology[11–13] prior to and after the catalytic testing.[5,9,10,14,15] Thus, we are in presence of a gap between morphology and catalytic performances.[8,16] To contribute in resolving this, the current study exploits the surface plasmon resonance (SPR) of metal nanoparticles in *operando* conditions, to characterize their size and structure in reaction conditions. In fact, since SPR originates from coherent excitations of the electronic density of metallic nanostructures, it is intrinsically strongly dependent upon size and shape of the metal nanoparticles.[17–19] In the growing field of nanoplasmonics, plasmons are used to enhance the electromagnetic field from an external source, and metal nanoparticles are synthetized *ad hoc* to allow local field effects at specific wavelengths of interest.[20,21] If this correspondence is univocal, the SPR shape-and-size dependency becomes a fingerprint to monitor the metal

[a] *Laboratory of Catalysis and Catalytic Processes, Dipartimento di Energia, Politecnico di Milano, Via la Masa 34, 20156 Milano, Italy. E-mail: matteo.maestri@polimi.it*
[b] *European Synchrotron Radiation Facility, 71 Avenue des Martyrs, CS 40220Grenoble, France*
[c] *Department of Chemistry, Materials and Chemical Engineering, Politecnico di Milano, Piazza Leonardo da Vinci 32, 20133, Milano, Italy*

† Electronic supplementary information (ESI) available. See DOI: https://doi.org/10.1039/d3cy01392h

nanoparticles morphological changes in reacting conditions. So far, this approach has been applied *ex situ*, to monitor the presence supported metal nanoparticles (*i.e.* for gold-based systems) on reducible (*i.e.* TiO_2, CeO_2) and non-reducible (*i.e.* Al_2O_3, SiO_2) oxides.[22] In this playground, the possibility to monitor in *operando* metal nanoparticles formation and their size and shape *via* Surface Plasmon Resonance on heterogeneous catalysts represent a novelty. In this article, we present an UV-vis spectroscopy study of Au-based catalysts, targeting the in-*operando* characterization of gold nanoparticles structure. In fact, nanostructured gold is characterized by a large number of conduction electrons easily polarized by an external electromagnetic field, *i.e.* induced by an UV-vis light source.[23] Hence, we employed an *ad hoc* developed UV-vis setup, to monitor the catalysts optical properties, aiming at gaining information on the size, shape, and stability of Au nanoparticles in a packed bed reactor, that is, with an *operando* approach. Furthermore, since gold nanoparticles have proven to be active for the *reverse* water gas shift (*r*WGS) reaction ($CO_2 + H_2 \leftrightarrow CO + H_2O$) when highly dispersed on a support,[24–26] we chose this reaction as a case study of the possibility to monitor the nanoparticle stability in reaction conditions. Thus, with the developed *operando* setup, we probed the behaviour of the formed Au nanoparticles in *operando*, exposing the catalyst to *r*WGS reaction conditions. X-ray absorption spectroscopy and synchrotron-based XRD are used as complementary techniques to witness the applicability of our experimental approach in studying the catalyst structure and behaviour. In parallel, HR-TEM and field-emission SEM (FESEM) allowed us to assess the shape of the formed Au nanoparticles, confirming our SPR-based methodology. On a general basis, these findings are of interest since direct information on the structure of metal sites at temperature and chemical conditions relevant for the catalytic application are obtained, with a novel approach to the field of metal-based supported catalysts characterization.

2 Experimental and methods

2.1 Materials

The Au-based materials studied in this paper were in-house synthetized. The $AuAl_2O_3$_30 and $AuAl_2O_3$_60 samples were prepared by direct impregnation of an α-Al_2O_3 support (Puralox, Sasol) with commercial colloidal suspensions of Au NPs with nominal diameter of 30 nm and 60 nm, respectively (HiQ-Nano, 1 mg_{Au} mL^{-1}). In total, 20 impregnations with the not diluted suspension were performed to obtain the 0.4% Au wt% loading. The 4 wt% $AuAl_2O_3$_4 catalyst was obtained by impregnation of the α-Al_2O_3 with a $HAuCl_4$ solution (Sigma-Aldrich, 99.99% au, 30 wt% in dilute HCl). The resulting powder was dried overnight at room temperature and was subsequently washed carefully to remove clorine. For each washing step (three performed with NH_3 (Sigma-Aldrich, 1 M) and five with H_2O, to restore the pH to 7) the powder was mechanically stirred until homogenization and centrifuged for 5 minutes at 4350 rpm. The washed powder was dried at room temperature and stored in dark conditions.

2.2 UV-vis spectroscopy *operando* setup

The *ex situ* and *operando* UV-vis spectra were measured coupling a powder reactor (Fig. 1) with a UV-vis diffuse reflectance probe, having six radiating optical fibers and one reading fiber. The data were recorded with the fiber always perpendicular to the investigated surface. The *operando* spectra were measured combining in an oven a high-temperature UV-vis reflectance probe with a powder reactor, to measure UV-vis spectra in reaction conditions. Thus, the experimental setup we developed allows us to measure the spectroscopic data while performing the targeted catalytic testing, with controlled temperature and gas feed. At variance with the spectroscopic cells usually utilized, our system allows for the acquisition of UV-vis spectra with the targeted sample directly placed in a tubular fixed-bed flow quartz reactor (5 mm internal diameter), designed to minimize the pressure drops and to avoid the mass transfer limitations. The reactants flow is passing through the entire catalytic bed height (from top to bottom), and the reactor can be vertically translated during the reaction, to monitor the optical properties of the sample in different positions along the catalytic bed. To exclude contributions from the specular reflectance (*i.e.* from the reactor outer walls) and to compensate for the possible absorption from quartz SiO and/or SiOH groups, the reference spectrum for the *operando* experiments is measured at room temperature (RT) in the same optical configuration. Thus, barium sulphate (chosen as white reference for both the *ex situ* and *operando* spectra) has been loaded in the quartz reactor, and placed inside the testing gas rig oven. This allows for the measurement of UV-

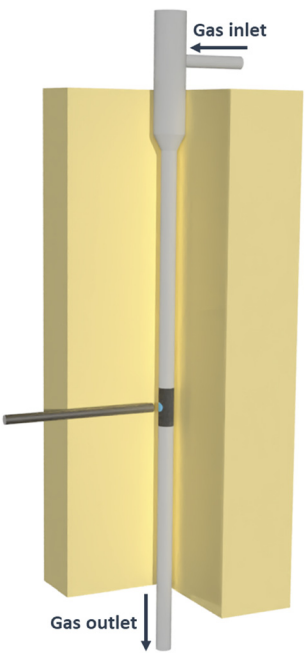

Fig. 1 Pictorial representation of the developed *operando* UV-vis setup combining the packed-bed reactor and the UV-vis probe.

vis data in reaction conditions without any modification to the reactor geometry and cross-section, thus avoiding any possible effect on the fluid dynamics. The *ex situ* and *operando* UV-vis spectra were recorded in the 200–1000 nm range at 1 nm resolution on a Exemplar Plus BTC655N spectrometer by B&W Tek, equipped with a black-thinned charge-coupled device (CCD) detector and B&W Tek BDS130A (deuterium–halogen) light source. Spectra are reported as relative reflectance (R%) defined as:

$$R\% = R_{sample}/R_{reference}$$

to avoid the possible artefacts connected to the use of the Kubelka–Munk function.[27–29]

Prior to the measurement, the sample is pelletized with a hydraulic press, successively chopped and sieved, selecting for the measurement the fraction between 75 and 106 μm. We have validated that the selected diameter range avoids any mass transfer limitations. The quartz reactor is loaded with ~200 mg of powder, and the catalyst bed is hold in place by a quartz wool support and by a sieved fraction of inert quartz (850 and 1160 μm). The temperature is controlled by a thermocouple (500 μm) placed inside the catalytic bed. The *operando* UV-vis experiments were performed during the reduction pretreatment (50 Ncc min^{-1} – 5% H_2/N_2 balanced) and during the *r*WGS catalytic testing (50 Ncc min^{-1}, CO_2/H_2 = 1, GHSV = 15 000 h^{-1}). The reaction was monitored over time, until the steady state was reached both in the spectra and in CO_2 conversion. Measurements were carried out from RT to 200/600 °C with a heating ramp of 2/5 °C min^{-1}, flowing the desired gases (H_2/N_2 or $CO_2/H_2/N_2$) with an *ad hoc* built gas flow setup. The setup consisted of four channels, each of them connected to a specific gas bottle and to a dedicated mass flow controller. The reaction products are monitored by means of an on-line gas cromatograph (Micro Gas Chromatograph GCX, Pollution).

2.3 X-ray absorption spectroscopy

X-ray Absorption Spectroscopy (XAS) data were collected at the BM31 beamline[30] of the European Synchrotron Radiation Facility (ESRF, Grenoble, France) using a quartz capillary with 1 mm external diameter, optimized for XAS data collection in transmission mode. The $AuAl_2O_3$_4 catalyst was pressed and sieved, and the 75 and 106 μm fraction was selected for the measurement. Au L_3-edge XAS measurements were performed in transmission mode, employing a double-crystal Si (111) monochromator for the incident energy scan, and ionization chambers to detect incident (I_0) and transmitted ($I_{1,2}$) photons. An Au metal foil was measured simultaneously using a third ionization chamber I_2, for energy calibration purposes.[31] XAS spectra of ~5 min each (energy range 11 800–12 950 eV; energy step = 0.5 eV; acquisition time of 70 ms per point in the whole energy range) were measured during the pretreatment in H_2 (10 Ncc min^{-1} – 5% H_2/He balanced) and during the *r*WGS reaction (10 Ncc min^{-1}, CO_2/H_2 = 1). The gas composition from the reactor outlet has been continuously monitored by means of a mass spectrometer (data not reported). The reaction was monitored over time, until the steady state was reached.

The Athena software (Demeter package)[32] was used to align XAS data by using the corresponding Au metal foil spectra and for normalization to unity of the edge jump. The same program was used for the extraction of the $\chi(k)$ function. R-Space FT-EXAFS spectra were obtained by calculating the Fourier transform of the $k^2\chi(k)$ functions in the (3.0–12.9) $Å^{-1}$ k-range.

2.4 Multivariate curve resolution-alternate least squares (MCR-ALS)

The time-resolved spectra are analyzed through the multivariate curve resolution-alternate least squares whose purpose is the resolution of the underlying contributions in unknown unresolved datasets.[33–35]

First, the identification of the number of *pure* species is obtained by Principal Component Analysis (PCA) of the experimental spectral dataset.[36,37] The number of correct principal components is evaluated by qualitative analysis, *i.e.* scree plot and R-factor, as well as by considering statistical tests, *i.e.* imbedded error function (IE-test), factor indicator function (IND-function) and Malinowski F-Test.[38]

MCR-ALS requires an initial estimate of either the concentration profiles or the spectra of *pure* components. Here, the simple-to-use interactive self-modeling mixture analysis (SIMPLISMA)[39] has been employed for obtaining the initial estimates of the *pure* spectra.

Once initial estimates are evaluated, MCR-ALS solves iteratively eqn (S10) and (S11) (as detailed in ESI† section 3) by alternating least square algorithm calculating the concentration profiles and the pure spectra optimally fitting the experimental data matrix. The optimization terminates when the difference between the model fit between two consecutive iterations does not significantly improve. During the optimization, to suppress the effect of rotational and scale ambiguities and fostering the physical/chemical meaningfulness, some constraints are introduced. In each of the iterative cycle, the computed profiles (concentrations, spectra) are modified to force to obey to the conditions imposed by some constraints.[40] Heren the non-negativity and mass conservation have been employed.

Additional details on the method and on the implementation are reported in ESI† sections 3 and 4.

2.5 PXRD, HRTEM and FESEM

***Operando*.** PXRD patterns were collected at the BM31 beamline of the ESRF, Grenoble, using a 45.786(1) keV monochromatic beam obtained from a sagittally focussing Si 111 double crystal monochromator. Diffracted intensities were collected by the means of a scintillation image plate detector (Dexela-Perkin Elmer 2923) having 3888 × 3072 pixels of 75 × 75 μm size whose position calibration was made by refining it against a NIST LaB_6 standard. Integration

of the images into 2D patterns was made with the software available and developed at the SNBL (Swiss Norwegian BeamLines) at the ESRF.[41]

HR-TEM analyses were performed by means of the high-resolution TEM JEOL JEM 3010-UHR, equipped with lanthanum hexaboride (LaB_6) light source, a nominal operating voltage of 300 kV and a theoretical resolution of 0.17 nm. The samples were prepared depositing the catalyst powder on a 3 mm copper grid. The HR-TEM images were analyzed using ImageJ, an open-source software. The particles size distribution was calculated counting on average more than 200 nanoparticles *per* sample. The FESEM analyses were carried out with a TESCAN S9000G microscope, which features a Schottky field emission gun and a resolution of 0.7 nm.

3 Results and discussion

3.1 *Operando* UV-vis spectroscopy

Using *ex situ* UV-vis diffuse reflectance (DR) spectroscopy, we validated the sensitivity of the SPR peak position to anchored nanoparticles dimensions. On the basis of this SPR experimental approach, we subsequently focused on monitoring *in situ* the formation of gold nanoparticles, and in *operando* their stability in reaction conditions.

It is here worth recalling that the SPR phenomenon arises from the light absorbed and scattered by a metal nanoparticle and it is quantitively evaluated through the respective cross section coefficient σ_{abs} and σ_{scat}.[42,43] The extinction cross section σ_{ext} is the sum of these contributions ($\sigma_{ext} = \sigma_{abs} + \sigma_{scat}$), and it shows a strong dependency on particle size.[44] This dependency results in a significative increase in absorbed light for even a moderate increase in the cross section values, that is, for an increase in the nanoparticles particle size, and in a damping when decreasing the nanoparticle dimensions.[17] Furthermore, the SPR peak position (*i.e.*, the maximum of the extinction cross-section) is also sensitive to the size of the nanoparticles. A red shift of the SPR peak accounts for increased dimensions of the nanoparticles, whereas a blue-shift corresponds to a nanoparticle size decrease.[5,17] The collective oscillations of electrons in the conduction band of gold atoms are thus responsible for the SPR peaks present in the spectra reported in Fig. S1,† measured for two Au/Al_2O_3 samples, obtained by direct impregnation of an α-Al_2O_3 with commercial suspensions of gold nanoparticles, having nominal diameter of 30 ($AuAl_2O_3$_30) and 60 ($AuAl_2O_3$_60) nm, respectively. The spectra show a minimum in the *R*% (*i.e.* the maximum of the extinction cross section) at different wavenumbers, as well as differences in the bandwidth. The $AuAl_2O_3$_60 curve presents a broad band centered at 540 nm, while the spectrum obtained for the $AuAl_2O_3$_30 sample, prepared with nanoparticles with a smaller diameter, presents a narrower band, sharper and more defined, centered at 530 nm. Since the position and intensity of Au SPR peaks depend on the size and shape of gold nanoparticles, and on the dielectric properties of the medium (*i.e.* the support), the observable differences between the experimental curves can be rationalized in terms of nanoparticles dimensions. In fact, we can rule out a major contribution on the SPR peak position from the dielectric constant of the surrounding means (air and α-Al_2O_3), as they are equal for both samples. The resolution the acquired spectra is ±1 nm, thus this experimental evidence highlights the potentiality of correlating the plasmon peak with metal nanoparticles dimensions, when anchored on a solid medium. The HR-TEM images (Fig. S2†) highlight that, in both samples, gold nanoparticles are mainly spherical. Furthermore, on average, gold nanoparticles are larger and with a broader distribution than the nominal one (38 ± 3 nm *vs.* 30 and 124.9 ± 8 nm *vs.* 60). Thus, as an increase in bandwidth and a red-shift of the SPR maximum is expected with the growth of nanoparticles size. The observed SPR λ_{max} shift between the $AuAl_2O_3$_30 and $AuAl_2O_3$_60 spectra can consequently be correlated with the differences in the average nanoparticle diameters obtained from HR-TEM. The observed shift in the SPR λ_{max} proved that monitoring the SPR peak position as a function of nanoparticle size is suitable to study metal nanoparticles on supported catalysts. Anchoring the metal nanoparticles on the Al_2O_3 support does not hinder the sensitivity of the SPR peak on the nanoparticles size.

With this approach, we studied a 4 wt% Au/Al_2O_3 sample (hereafter $AuAl_2O_3$_4) during the thermal treatment in H_2 (5% H_2/N_2, 50 Ncc min^{-1}) from RT to 200 °C, which has been reported as optimal to obtain active gold catalysts.[45] Indeed, the H_2-reduction treatment results in the formation of gold nanoparticles, highlighted by the presence of a visible SPR peak in the spectrum measured at 200 °C (red curve in Fig. 2). Comparing the SPR λ_{max} centered at 540 nm and the bandwidth with the spectra measured *ex situ*, we can infer that the formed gold nanoparticles present a broad size distribution, and/or are present as aggregates (*i.e.* by

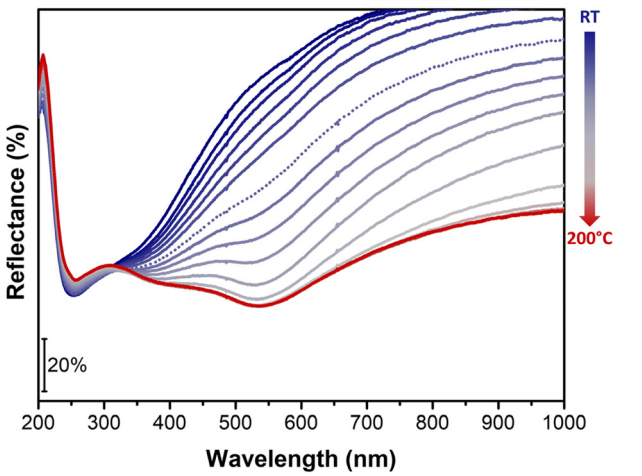

Fig. 2 *In situ* UV-vis DR spectra of $AuAl_2O_3$_4 during H_2-pretreatment from RT to 200 °C (blue to red curves); blue dotted curve: spectrum at *ca.* 135 °C.

comparison with the $AuAl_2O_3$_60 spectrum). The broadening of the SPR peak in the *in situ* spectrum, might be related to the concomitant thermal excitation of the free electrons of gold, in parallel with the generation of the plasmon wave when working at high temperature. The FESEM results reported in Fig. 3a show that the sample is characterized by small, isolated gold nanoparticles and larger agglomerates, which present a raspberry-like structure. These agglomerates have a size ranging between 15 and 100 nm and are formed by nanoparticles that are still separated and have not collapsed and/or coalesced (see Fig. 3c). From the HR-TEM images in Fig. 3b and c, we can observe that Au nanoparticles in the agglomerates have a slightly different shape when compared to the isolated ones. In fact, it is clearly visible that the agglomerated nanoparticles present a more spherical shape (Fig. 3c), while the majority of the observed isolated nanoparticles is characterized by a well-defined cubo-octahedral shape (Fig. 3b), which has been reported to be the most energetically favoured structure for gold nanoparticles with diameters higher that 3 nm.[5,6,46,47]

Furthermore, we observed that Au particles on average expose [2,0,0] and [1,1,1] lattice planes, as visible in Fig. 3d, which are the main expected crystallographic reflexes for nano-structured gold.[45] These findings are in agreement with the PXRD data (Fig. S3†) measured for the $AuAl_2O_3$_4. The diffractograms present very sharp peaks clearly ascribable to the support (crystalline α-Al_2O_3 or corundum (ICSD entry no. 9770)[48]) which is mostly unperturbed by the H_2 pre-treatment. The observable minor peak shifts and intensity changes are due to the lattice thermal expansion and the increase of the atom thermal motions. In parallel, we observe the appearance of a new phase, that is, fcc metallic Au (ICSD entry no. 64 701), presenting the characteristic reflexes at 6.6° for the [1,1,1] lattice plane, at 7.63° for [2,0,0], and at 10.08° for [2,2,0]. Minor signals related to the [3,1,1] and [2,2,2] lattice planes are also visible at higher θ values. The interplanar distances (0.204 nm and 0.238 nm) calculated from HR-TEM images (Fig. 3d) are in accordance with the peaks visible in the PXRD pattern and correspond to the most abundant [2,0,0] and [1,1,1] facets. The average nanoparticles size has been evaluated from HR-TEM images, resulting to be of 5.99 ± 0.13 nm in agreement with literature values (Fig. 3e),[5,25,46,49] with a quite narrow distribution (less than 10% nanoparticles have diameters between 8–10 nm and less than 8% have an average size of $10 \leq d \leq 16$). Thus, the general intense broadening of all diffraction peaks is due to the size of the Au nanoparticles, as highlighted by TEM imaging. Despite the narrow particle size distribution, the sample has an intrinsic heterogeneity (*i.e.* the presence of larger agglomerates) mirrored by the observed SPR spectral features, which can then be considered representative of the average gold speciation.

It is now noteworthy to mention that initially gold is present on the alumina surface as isolated Au^{3+} ions, resulting from the impregnation of the α-Al_2O_3 with the gold precursor. Indeed, the initial spectrum measured in H_2 at RT (dark blue curve in Fig. 2) is characterized by a broad absorption below 600 nm, which is likely to be related to the Ligand-to-Metal (L → M) Charge Transfer transitions, in agreement with features observed on similar Au^{3+} complexes.[50] Specifically, it is reasonable to assign the band at 450 nm (measured at half height) to electronic transitions from the O atoms present in the gold coordination sphere (O → Au^{3+}). The observed charge–transfer transitions are at lower energy when

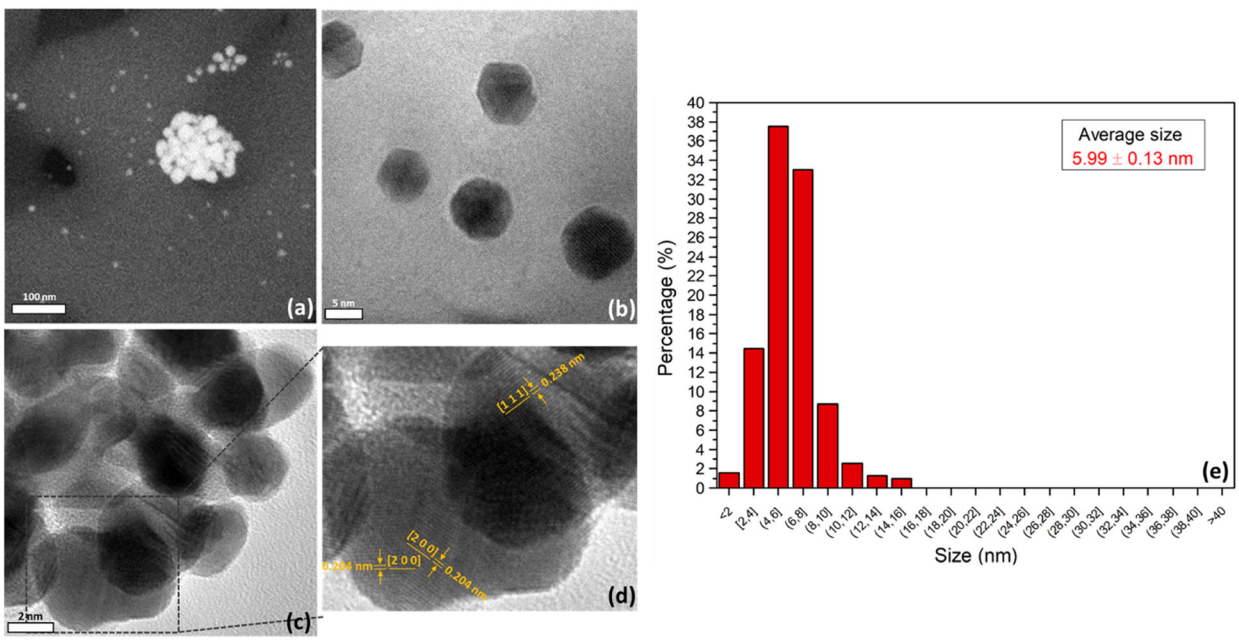

Fig. 3 (a) FESEM and (b) and (c) HRTEM images of $AuAl_2O_3$_4; (d) magnification of gold nanoparticles in (c) with highlighted lattice planes; (e) NPs size distribution of $AuAl_2O_3$_4.

compared to those reported for $[AuCl_4]^-$ complexes in literature,[5] in agreement with the position of oxygen and OH groups in the spectrochemical series of ligands. The observable features below 270 nm, which falls in the spectral region where the electronic transitions of Au^+ are expected,[51] are in our case instead related to the absorption from the quartz wall reactor.

When increasing the temperature from RT to 200 °C in H_2 feed, we can observe a progressive rearrangement of the chemical species on the catalyst surface. In fact, the progressive broadening of the LMCT transitions band and the decrease in reflectance can possibly stem for the formation of some multimerics Au clusters on the Al_2O_3 surface. With the progressive temperature increase, an inflection point at about 550 nm starts to appear (Fig. 2, blue dotted curve, *ca.* 135 °C) which suggests the initial formation of gold nanoparticles (*i.e.* around 2 nm).[17] These nanoparticles act as nuclei for the growth of larger ones, as the $Au^{3+} \rightarrow Au^0$ reduction proceeds, until all the gold is present on the Al_2O_3 surface as Au^0. At high temperature, the changes observed in the 200–300 nm range are related to a worse background compensation.

3.2 X-ray absorption spectroscopy and MCR-ALS analysis

To further corroborate the developed experimental approach in monitoring the formation of gold nanoparticles, we followed $Au^{3+} \rightarrow Au^0$ reduction by means of X-ray absorption spectroscopy. The resulting Au L_3 XANES spectra, measured during the 5% H_2-pretreatment, are reported in Fig. 4a (from dark blue to red curves). The Au L_3 XANES are known to be sensitive not only to the oxidation state of the X-ray absorber atom, but also to the electronegativity, the type and the symmetry of the ligands, thus being a complementary technique to the applied UV-vis DR. The first spectrum (dark blue curve) presents an intense white line feature around 11 920 eV, typical of the Au^{3+} oxidized state of gold. The Au^{3+} white line is shifted to lower energies, at variance with the higher energies usually measured for oxidized species. This is ascribable to the 2s → 5d dipole-allowed transitions, that anticipate the excitation of the bulk electrons, and correlates with the number of holes in Au 5d band.[52–54] Duggar at about 100 °C, the intensity in the white line region started to decrease and the edge position shifts to higher energies, stemming for a change in Au^{3+} oxidation state. The changes in the white line area might be associated with changes in the ionicity and/or electron transfer between the absorbing atom and the ligands. Moreover, between 11 930 eV and 11 955 eV, we can observe the growth of new features, while those between 11 955 eV and 11 980 eV tends to decrease. The observed behaviour is associated with the progressive conversion of the oxidized Au^{3+} species to Au^0. The spectrum at 200 °C (red curve) closely resemble that of metallic gold, with less intense features,[52,53,55] accounting for a lower Au average coordination number. The absence of the white line in the spectrum of metallic gold results from its electronic configuration, as Au^0 ($5d^{10}$, $6s^2$) has the *d* level completely filled.[56,57]

To clarify the dynamics of the $Au^{3+} \rightarrow Au^0$ reduction, we performed MCR-ALS analysis on the XANES spectra (additional details in ESI† section 4). The first step of the analysis involved the determination of the number of pure

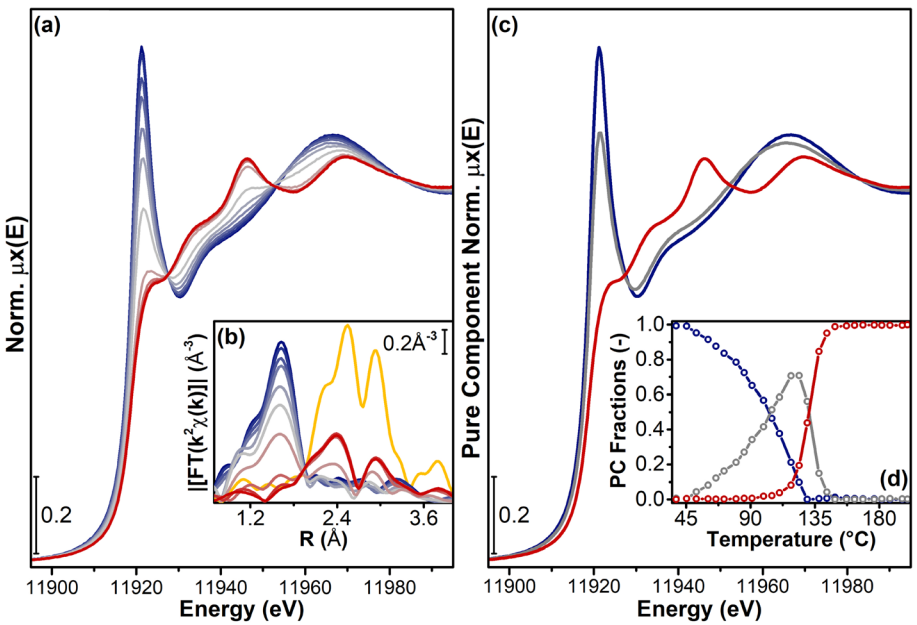

Fig. 4 (a) *Operando* XANES and (b) EXAFS during H_2-pretreatment from RT to 200 °C (dark blue to red curves; yellow curve in (b): EXAFS spectrum of bulk gold); (c) XANES spectra of pure components ($\mu_i^{pure}(E)$) derived from MCR-ALS analysis of temperature-dependent XANES dataset during H_2-pretreatment from RT to 200 °C, assuming N_{PC} = 3 and (d) concentration profiles of the Au-species corresponding to the pure XANES spectra.

components. To this aim, we performed principal component analysis (PCA) of the XANES dataset (see ESI† section 3). From qualitative analysis based on the abstract components (see Fig. S6†) and the *R*-factor (see Fig. S7†) as well as statistical analysis, we identified the presence of three principal components (see Fig. S8†). The selection of N_{pure} could strongly influence the MCR-ALS results. Hence, we repeated the analysis for downsizing the component space equal to 2. The results are reported in ESI† section 5. The analysis revealed that the number of pure components identified by statistical analysis, N_{pure} = 3, represents an optimal value-resolution. The results from MCR-ALS analysis are reported in Fig. 4, in terms of pure XANES spectra and concentration profiles (Fig. 4c and d, respectively). Considering the observable XANES features of the MCR spectra, we can identify the presence of three Au species, characterized by different oxidation states. We assign the blue spectrum in Fig. 4b, characterized by an intense white line feature and by the edge position at lower energies to an Au^{3+} oxidized species. The red curve in Fig. 4c shows similar features to that of metallic gold and is assigned to Au^0. The third component is characterized by a white line feature of lower intensity and by an edge position shifted to higher energy. We hypothesize that this species is an $Au^{\delta+}$ intermediate, which is formed during the progressive reduction and rearrangements of Au atom on the Al_2O_3 surface. This is in agreement with the behaviour observed in the UV-vis spectra, which are characterized by progressive changes in the LMCT region, stemming for changes in the ligand coordination sphere and bond character of the absorber atoms, as a result of the progressive $Au^{3+} \rightarrow Au^0$ reduction. The corresponding relative concentration profiles of the formed species (see Fig. 4c) further underline the formation and the consumption of the $Au^{\delta+}$ intermediate (grey line in Fig. 4d) as the reduction of Au^{3+} proceeds. In fact, we can observe that the concentration of Au^{3+} species starts to decrease shortly after feeding the reactive gas feed (see blue line in Fig. 4d), with the concomitant growth of the $Au^{\delta+}$ intermediate. This species reaches a maximum around 125 °C, with a subsequent sharp decrease, related to its progressive reduction to Au^0. The temperature at which the concentration of Au^0 starts to increase at the expenses of $Au^{\delta+}$ (*ca.* 135 °C) corresponds to the temperature at which we observed the appearance of the initial SPR feature in the UV-vis spectrum (blue dotted line in Fig. 2). This results in a fair agreement in the description of the evolution of the investigated system between the two applied experimental approaches. Above 135 °C, Au^0 becomes the most prevalent species anchored on Al_2O_3.

Fourier transformed (FT) Extended X-ray Absorption Fine Structure (EXAFS) provides additional information on the formed gold nanoparticles. EXAFS spectra measured during H_2-pretreatment are reported in Fig. 4b. The dark blue spectrum (Fig. 4b) corresponds to the catalyst precursor just before the activation. In accordance with literature,[53] it closely resembles the spectrum of Au_2O_3, further confirming that, prior to the thermal treatment, the as-prepared sample contain isolated Au^{3+} species. Specifically, the absence of any peaks associated to Au–Au backscattering features excludes the presence of Au^0, while the peak at 1.6 Å is related to the presence of oxygen or nitrogen atoms in the first coordination shell of Au. During the H_2-pretreatment we can observe the progressive decrease of the first shell feature, with the growth of two peaks assigned to Au–Au backscattering amplitude. Thus, the reduction in hydrogen led to the formation of Au–Au shell at expense of the initial Au–O or Au–N one and the final spectrum (red curve in Fig. 4b) is similar to the one of bulk gold (yellow curve in Fig. 4b). The EXAFS spectrum of bulk gold presents two intense peaks at around 2.5 Å and 3 Å, respectively linked to the first Au coordination shell, characterized by the presence of 12 Au neighbouring atoms (approximate Au–Au distance 2.85 Å) and to the second shell of 6 atoms (approximate Au–Au distance 4.08 Å). The different intensity in the EXAFS features between the yellow and red curves proves the lower coordination number for Au in our sample, confirming the average small dimensions of the gold nanoparticles formed, in line with the HR-TEM and PXRD findings. The results reported so far allow for the description of the average gold speciation, highlighting the possibility to exploit the SPR to monitor the formation of gold nanoparticles with well-defined shapes and sizes.

3.3 SPR monitoring in *operando* during CO_2 activation

To showcase the SPR monitoring in conditions relevant for the catalysis, we exposed the $AuAl_2O_3$_4 catalyst to a mixture of CO_2 and H_2. We selected the reverse water gas shift reaction (*r*WGS, $CO_2 + H_2 \leftrightarrow CO + H_2O$)), since supported gold nanoparticles are active hydrogenation catalysts.[58,59] This reaction on Au-based catalysts proceeds *via* associative mechanism, that is, H_2 is dissociatively chemisorbed on Au^0 while CO_2 is activated on the Al_2O_3 surface. The spillover of H* species on the support allows for the formation of

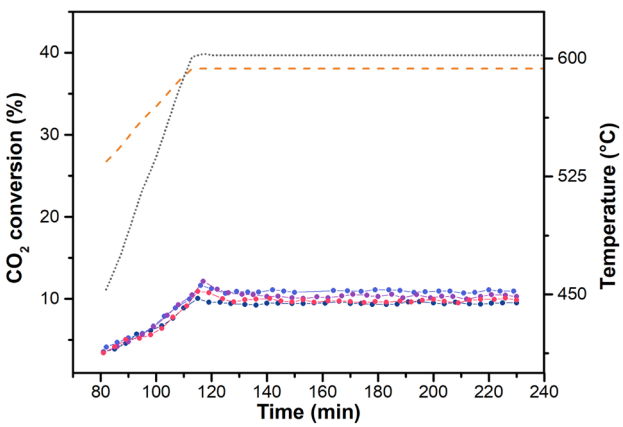

Fig. 5 CO_2 conversion on $AuAl_2O_3$_4; (colour code: test 1, light blue; test 2; test 3, purple; test 4, black; dashed orange line: equilibrium); temperature profile reported as grey dotted line.

reaction intermediates (*i.e.* formates) that decompose to CO and H_2O.[25]

Fig. 5 shows CO_2 conversion as a function of the reaction temperature and time-on-stream for four *r*WGS tests under stoichiometric conditions (5% H_2, 5% CO_2 and 90% N_2, GHSV = 15 000 Nl kg_{cat}^{-1} h^{-1}), from RT to 600 °C. In all the performed tests, CO_2 conversion increased with temperature and remained well below the thermodynamic value (see orange curve in Fig. 5). The reported catalytic results allowed us to observe that the catalyst was active, with CO_2 conversion values at 600 °C that slightly oscillate around a value of 9.5%.[25,60] Throughout the reaction CO was the sole product measured, with no traces of CH_4 or other oxygenated side products, thus highlighting a high CO selectivity on Au-based catalysts.[25,60] Fig. 6a reports the UV-vis DR spectra measured during the RT-600 °C temperature ramp under stochiometric *r*WGS conditions (from red to light blue curves). Feeding the reactive gas mixture on the sample does not alter the SPR peak priorly formed (see red curve in Fig. 6a), which remains well-defined. As the reaction temperature increases, the *operando* spectra are characterized by a progressive broadening and red-shift of the observable SPR peak (from 540 nm, after the *in situ* H_2-pretreatment, to 550 nm). Once reached 600 °C, we do not observe any further changes in the UV-vis spectra over time (see dashed purple line in Fig. 6a, measured after 230 minutes). The SPR peak remains stable and symmetric during the reaction, stemming for a preserved regular morphology of gold nanoparticles and for the absence of major agglomeration phenomena. In fact, the observed SPR peak broadening and the consequent λ_{max} SPR red-shift might be primarily related to the temperature increase, which induces a strong excitation in the Au nanoparticles surface electrons and a thermal dilatation of Au lattice.[17] These hypotheses have been confirmed by the HR-TEM analysis on the spent catalyst (Fig. S5†), which is characterized by small, isolated nanoparticles, with many neighbouring agglomerates with the peculiar raspberry-like shape as the fresh catalyst. The average nanoparticle sizes between the two samples are comparable (6.67 ± 0.10 nm *vs.* 5.99 ± 0.13 nm) as the size distributions, since 90% of nanoparticles have a dimension lower than 10 nm. These findings allowed us to prove the feasibility of the developed experimental approach in monitoring metal nanoparticles size in reaction conditions.

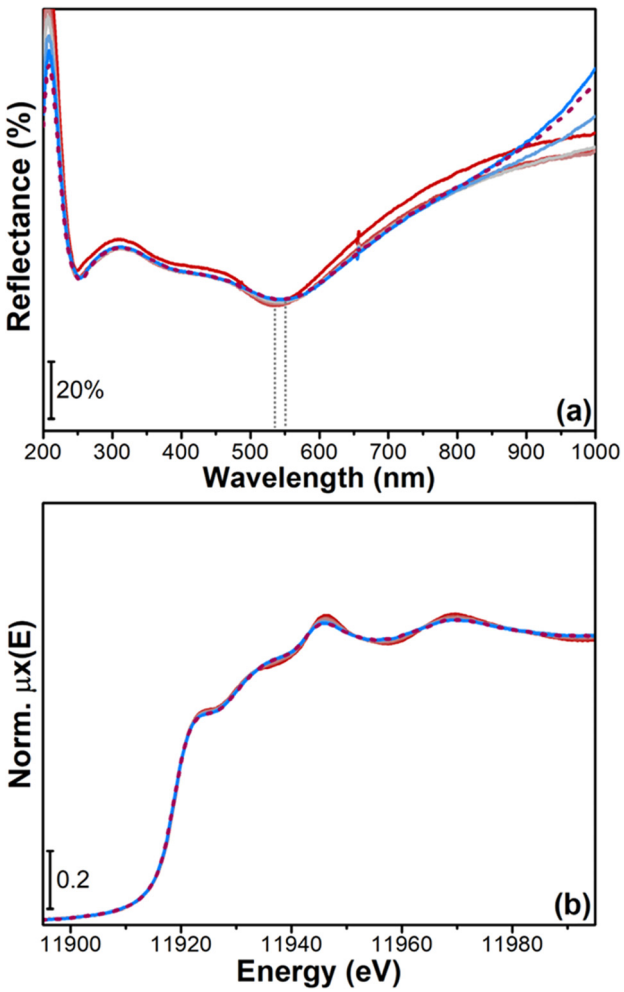

Fig. 6 (a) *Operando* UV-vis DR spectra during *r*WGS from RT to 600 °C (from red to light blue curves) and after 230 minutes in isotherm at 600 °C (dashed purple curve); (b) *operando* XANES spectra during rWGS from RT to 600 °C (from red to light blue curves) and after 230 minutes in isotherm at 600 °C (dashed purple curve). The grey dotted lines highlight the shift in the SPR peak position.

Moreover, the reactivity towards CO_2/H_2, monitored in parallel by *operando* XANES (Fig. 6b), resulted to be in agreement with the UV-vis data. The spectra measured during the temperature ramp from RT to 600 °C and in isotherm at 600 °C are reported in Fig. 6b. The changes visible in Au L_3 post-edge features during the *r*WGS ramp from RT to 600 °C (from red to light blue curves) can be again associated with the temperature increase, which promotes electron mobility and causes the broadening of the observed XANES features. There are no changes in the pre-edge and white line region, thus confirming that, during reaction, the sample preserves its Au^0 oxidation state. Furthermore, from a qualitative analysis of the XANES spectra, we can infer that sintering does not occur significantly, since this phenomenon would change the average coordination number of Au atoms, thus modifying the features visible in the XANES spectra towards those of bulk gold.[52] In agreement with the *operando* UV-vis data, the XANES spectrum measured after 230 minutes (purple dashed line in Fig. 6b) show the catalyst stability over time in the applied experimental conditions.

Indeed, from the spectroscopic data reported it emerges the feasibility of using the SPR peak as a marker of the metal oxidation state and of the nanoparticles size, with the possible further support of advances characterization techniques such as *operando* XAS. The results obtained validating the technique on gold nanoparticles can be applied to any metals presenting the SPR phenomenon in the selected spectral range.

4 Conclusions

In this study, we have introduced surface plasmon resonance (SPR) as a distinctive marker for the morphology of supported metal nanoparticles in conditions pertinent to catalysis. Utilizing *ex situ* UV-vis spectroscopy, we examined the SPR characteristics of gold nanoparticles on α-Al_2O_3, demonstrating the capability of SPR to track changes in nanoparticle size under reaction conditions. *Operando* UV-vis spectroscopy allowed us following the dynamics of nanoparticles formation and of their reactivity during the reverse water gas shift reaction. We monitored the progressive change in coordination of Au^{3+} ions through the development of the SPR peak, and the subsequent stability of the formed gold nanoparticles in reaction conditions. Namely, the SPR peak position of supported gold nanoparticles was found to be affected both by the nanoparticle dimensions and the presence of agglomerates. The catalytic results measured during the *operando* UV-vis experiment evidenced a good activity for *r*WGS of the Au catalyst, with a 100% CO selectivity. *Operando* XAS and PXRD data confirmed the experimental evidences from UV-vis spectroscopy, showing that Au nanoparticles are formed with very small size and are stable in reacting feed. Our findings validate the potential of using SPR for studying the morphology of catalysts. This method could be effectively applied to other supported-metal catalysts that exhibit SPR phenomena, such as Pt, Ag, and Cu. Furthermore, the technique can be applied as a design-of-experiment methodology to properly select and screen the measurements to be performed at large scale facilities (synchrotron), aiming at optimizing data acquisition and material characterization. Overall, the developed approach allows for the direct investigation of metal-based supported catalysts, gaining direct information on the structure–activity relation under catalysis relevant conditions.

Conflicts of interest

There are no conflicts to declare.

Acknowledgements

The authors acknowledge funding from MIUR (Italy) – FARE (Framework per l'attrazione e il rafforzamento delle eccellenze per la ricerca in Italia) – project SPOON (Surface Plasmon resOnance for the in-*Operando* characterization of shape and size of supported metallic Nanoparticles), prot. number R16RNP82WW and from the European Union's Horizon 2020 research and innovation programme under grant agreement no. 966758 (ERC-PoC project SPECTROKIN). The European Synchrotron Radiation Facility (ESRF, Grenoble, France) is acknowledged for beamtime allocation on BM31 beamline and we would like to thank Dr. Stoian for the assistance and support in using BM31 beamline. The authors are deeply indebted to Dr. Valsania and Dr. Rebba for the HR-TEM and FESEM measurements. The authors are thankful to F. Alleva for the support in the development of the UV-vis setup, and for the UV-vis spectra acquisition and data elaboration.

References

1 M. P. Dudukovic, *Science*, 2009, **325**, 698–701.
2 T. Van Gerven and A. Stankiewicz, *Ind. Eng. Chem. Res.*, 2009, **48**, 2465–2474.
3 G. Gert, *Nobel Lecture in Chemistry*, 2007.
4 Z. Hu, J. Han, Y. Wei and Z. Liu, *ACS Catal.*, 2022, **12**, 5060–5076.
5 A. Villa, N. Dimitratos, C. E. Chan-Thaw, C. Hammond, G. M. Veith, D. Wang, M. Manzoli, L. Prati and G. J. Hutchings, *Chem. Soc. Rev.*, 2016, **45**, 4953–4994.
6 H. Yoshida, Y. Kuwauchi, J. R. Jinschek, K. J. Sun, S. Tanaka, M. Kohyama, S. Shimada, M. Haruta and S. Takeda, *Science*, 2012, **335**, 317–319.
7 B. Weckhuysen, in *In situ Spectroscopy of Catalysts*, American Scientific Publishers, 2004 ch. 11, pp. 1–11.
8 A. Chakrabarti, M. E. Ford, D. Gregory, R. Hu, C. J. Keturakis, S. Lwin, Y. Tang, Z. Yang, M. Zhu, M. A. Bañares and I. E. Wachs, *Catal. Today*, 2017, **283**, 27–53.
9 M. Manzoli, F. Boccuzzi, A. Chiorino, F. Vindigni, W. L. Deng and M. Flytzani-Stephanopoulos, *J. Catal.*, 2007, **245**, 308–315.
10 M. Manzoli, A. Chiorino and F. Boccuzzi, *Surf. Sci.*, 2003, **532**, 377–382.
11 F. Vindigni, M. Manzoli, A. Chiorino and F. Boccuzzi, *Gold Bull.*, 2009, **42**, 106–112.
12 F. Menegazzo, F. Pinna, M. Signoretto, V. Trevisan, F. Boccuzzi, A. Chiorino and M. Manzoli, *ChemSusChem*, 2008, **1**, 320–326.
13 S. Mourdikoudis, R. M. Pallares and N. T. K. Thanh, *Nanoscale*, 2018, **10**, 12871–12934.
14 M. Shekhar, W. S. Lee, M. C. Akatay, L. Maciel, W. J. Tang, J. T. Miller, E. A. Stach, M. Neurock, W. N. Delgass and F. H. Ribeiro, *J. Catal.*, 2022, **405**, 475–488.
15 M. Shekhar, J. Wang, W.-S. Lee, W. D. Williams, S. M. Kim, E. A. Stach, J. T. Miller, W. N. Delgass and F. Ribeiro, *J. Am. Chem. Soc.*, 2012, **134**, 4700–4708.
16 A. Urakawa, *Curr. Opin. Chem. Eng.*, 2016, **12**, 31–36.
17 V. Amendola, R. Pilot, M. Frasconi, O. M. Marago and M. A. Iati, *J. Phys.: Condens. Matter*, 2017, **29**, 203002.
18 V. Amendola, S. Polizzi and M. Meneghetti, *J. Phys. Chem. B*, 2006, **110**, 7232–7237.
19 A. M. Watson, X. Zhang, R. A. de la Osa, J. M. Sanz, F. Gonzalez, F. Moreno, G. Finkelstein, J. Liu and H. O. Everitt, *Nano Lett.*, 2015, **15**, 1095–1100.
20 V. Myroshnychenko, J. Rodriguez-Fernandez, I. Pastoriza-Santos, A. M. Funston, C. Novo, P. Mulvaney, L. M. Liz-Marzan and F. J. G. de Abajo, *Chem. Soc. Rev.*, 2008, **37**, 1792–1805.
21 C. M. Cobley, S. E. Skrabalak, D. J. Campbell and Y. N. Xia, *Plasmonics*, 2009, **4**, 171–179.
22 Y. Borensztein, L. Delannoy, A. Djedidi, R. Barrera and C. Louis, *J. Phys. Chem. C*, 2010, **114**, 9008–9021.

23 V. Amendola and M. Meneghetti, *J. Phys. Chem. C*, 2009, **113**, 4277–4285.
24 M. Ziemba, J. Weyel and C. Hess, *Appl. Catal., A*, 2022, **301**, 120825.
25 L. F. Bobadilla, J. L. Santos, S. Ivanova, J. A. Odriozola and A. Urakawa, *ACS Catal.*, 2018, **8**, 7455–7467.
26 T. V. W. Janssens, B. S. Clausen, B. Hvolbaek, H. Falsig, C. H. Christensen, T. Bligaard and J. K. Norskov, *Top. Catal.*, 2007, **44**, 15–26.
27 C. Negri, M. Signorile, N. G. Porcaro, E. Borfecchia, G. Berlier, T. V. W. Janssens and S. Bordiga, *Appl. Catal., A*, 2019, **578**, 1–9.
28 F. C. Jentoft, *Adv. Catal.*, 2009, **52**, 129–211.
29 F. C. Meunier, *React. Chem. Eng.*, 2016, **1**, 134–141.
30 O. Mathon, A. Beteva, J. Borrel, D. Bugnazet, S. Gatla, R. Hino, I. Kantor, T. Mairs, M. Munoz, S. Pasternak, F. Perrin and S. Pascarelli, *J. Synchrotron Radiat.*, 2015, **22**, 1548–1554.
31 S. Bordiga, E. Groppo, G. Agostini, J. A. van Bokhoven and C. Lamberti, *Chem. Rev.*, 2013, **113**, 1736–1850.
32 B. Ravel and M. Newville, *J. Synchrotron Radiat.*, 2005, **12**, 537–541.
33 A. de Juan and R. Tauler, *Anal. Chim. Acta*, 2003, **500**, 195–210.
34 A. de Juan and R. Tauler, *Crit. Rev. Anal. Chem.*, 2006, **36**, 163–176.
35 R. Tauler, *Chemom. Intell. Lab. Syst.*, 1995, **30**, 133–146.
36 C. Ruckebusch, *Data Handl. Sci. Technol.*, 2016, **30**, 1–4.
37 J. Timoshenko and A. I. Frenkel, *ACS Catal.*, 2019, **9**, 10192–10211.
38 A. Martini and E. Borfecchia, *Crystals*, 2020, **10**, 664.
39 W. Windig, C. E. Heckler, F. A. Agblevor and R. J. Evans, *Chemom. Intell. Lab. Syst.*, 1992, **14**, 195–207.
40 J. Jaumot, R. Gargallo, A. de Juan and R. Tauler, *Chemom. Intell. Lab. Syst.*, 2005, **76**, 101–110.
41 V. Dyadkin, P. Pattison, V. Dmitriev and D. Chernyshov, *J. Synchrotron Radiat.*, 2016, **23**, 825–829.
42 S. A. Maier, *Plasmonics: fundamentals and applications*, Springer, 2007.
43 U. Kreibig and M. Vollmer, in *Optical properties of metal clusters*, Springer, 1995, pp. 13–201.
44 T. Biwa, M. Yui, T. Takeuchi and U. J. M. T. Mizutani, *Mater. Trans.*, 2001, **42**, 939–950.
45 A. C. Gluhoi, X. Tang, P. Marginean and B. E. Nieuwenhuys, *Top. Catal.*, 2006, **39**, 101–110.
46 P. D. Srinivasan, H. D. Zhu and J. J. Bravo-Suarez, *Mol. Catal.*, 2021, **507**, 111572.
47 A. S. Barnard, X. M. Lin and L. A. Curtiss, *J. Phys. Chem. B*, 2005, **109**, 24465–24472.
48 L. W. Finger and R. M. Hazen, *J. Appl. Phys.*, 1978, **49**, 5823–5826.
49 J. Hernandez, J. Solla-Gullon, E. Herrero, J. M. Feliu and A. Aldaz, *J. Nanosci. Nanotechnol.*, 2009, **9**, 2256–2273.
50 T. M. Salama, T. Shido, R. Ohnishi and M. Ichikawa, *Zh. Fiz. Khim.*, 1996, **100**, 3688–3694.
51 J. L. Margitfalvi, A. Fasi, M. Hegedus, F. Lonyi, S. Gobolos and N. Bogdanchikova, *Catal. Today*, 2002, **72**, 157–169.
52 E. Bus, R. Prins and J. van Bokhoven, *Phys. Chem. Chem. Phys.*, 2007, **9**, 3312–3320.
53 L. Delannoy, N. Weiher, N. Tsapatsaris, A. M. Beesley, L. Nchari, S. L. Schroeder and C. Louis, *Top. Catal.*, 2007, **44**, 263–273.
54 J. W. Watkins, R. C. Elder, B. Greene and D. W. Darnall, *Inorg. Chem.*, 1987, **26**, 1147–1151.
55 N. Weiher, E. Bus, L. Delannoy, C. Louis, D. E. Ramaker, J. Miller and J. van Bokhoven, *J. Catal.*, 2006, **240**, 100–107.
56 G. Corro, S. Cebada, U. Pal and J. L. G. Fierro, *J. Catal.*, 2017, **347**, 148–156.
57 H. Duggal, P. Rajput, I. Alperovich, T. Asanova, D. Mehta, S. N. Jha and S. Gautam, *Vacuum*, 2020, **176**, 109294.
58 J. Guzman and B. C. Gates, *Am. Ethnol.*, 2003, **115**, 714–717.
59 S. A. Jimenez-Lam, M. G. Cardenas-Galindo, B. E. Handy, S. A. Gomez, G. A. Fuentes and J. C. Fierro-Gonzalez, *J. Phys. Chem. C*, 2011, **115**, 23519–23526.
60 M. González-Castaño, B. Dorneanu and H. Arellano-García, *React. Chem. Eng.*, 2021, **6**, 954–976.